

# Tailoring Rigid Segments in Dopant-Free Polymeric Hole Transport Materials for Perovskite Quantum Dot Solar Cells

Dae Hwan Lee,<sup>#</sup> Seyeong Lim,<sup>#</sup> Chanhyeok Kim, Han Uk Lee, Dasol Chung, Yelim Choi, Jongmin Choi, Younghoon Kim, Sung Beom Cho,\* Hong Il Kim,\* and Taiho Park\*



Cite This: *ACS Energy Lett.* 2023, 8, 1839–1847



Read Online

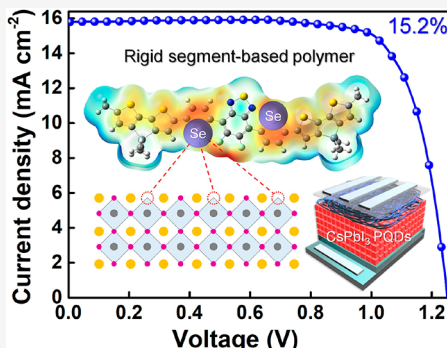
ACCESS |

Metrics & More

Article Recommendations

Supporting Information

**ABSTRACT:** The dominant hole transport material (HTM) used in perovskite quantum dot solar cells (PQD-SCs) is a Spiro-OMeTAD, which inevitably requires doping systems to increase charge mobility. However, the use of deliquescent dopants leads to the degradation of PQD-SCs, necessitating the development of efficient dopant-free HTMs for their commercialization. Here, we designed three types of dopant-free HTMs: Asy-PDTS, Asy-PSDTS, and Asy-PSeDTS. We apply chalcogenide-based fluorinated benzothiadiazole as a rigid segment acceptor unit to generate an effective charge hopping channel, compensating for the impaired electrical property through side chain engineering. The rigid segment is constructed into favorable planar structures of face-to-face stacking by a conformation-locking approach via chalcogenide–fluorine non-covalent interactions (S···F and Se···F). The optimized device using Asy-PSeDTS achieved 15.2% power conversion efficiency (PCE) and maintained 80% of the initial PCE after 40 days, which is the highest PCE and stability among dopant-free HTM-based PQD-SCs so far.



**C**sPbI<sub>3</sub> perovskite quantum dots (PQDs) are promising absorbers with strong light absorption, excellent optical properties, and a tunable bandgap.<sup>1–5</sup> However, CsPbI<sub>3</sub> PQDs suffer from stability issues, as they can transition from the photoactive phase ( $\alpha$ -CsPbI<sub>3</sub>) to the photoinactive phase ( $\delta$ -CsPbI<sub>3</sub>) when exposed to moisture or oxygen.<sup>6–10</sup> This is because of the surface traps of PQDs generated by incomplete dynamic ligand exchange,<sup>10,11</sup> which are necessary for improving the electrical coupling between PQDs. To overcome this issue, surface manipulation methods such as ligand treatment,<sup>12–15</sup> compositional engineering,<sup>16,17</sup> and the heterostructure strategy<sup>10,11,18–20</sup> have been introduced for passivating the PQD surface.

Compared with impressive progress in PQD absorbers, the development of hole transport materials (HTMs) has not been thoroughly explored in this field, despite their crucial role in surface passivation and device performance. So far, most perovskite solar cells (PSCs) adopt Spiro-OMeTAD, which has insufficient hole mobility. Therefore, dopants such as lithium salt and *tert*-butylpyridine are employed to enhance the charge transport property.<sup>21,22</sup> These deliquescent dopants induce moisture and penetrate perovskite crystals, accelerating the degradation of PQDs (Figure S1). To address these limitations, Ma et al.<sup>23</sup> reported PQD solar cells (PQD-SCs) employing commercially available dopant-free conjugated

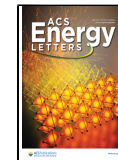
polymers (such as PTB7, PTB7-Th, and P3HT), but the corresponding devices still exhibit low efficiencies. Therefore, developing a new dopant-free HTM is essential to commercializing PQD-SCs.

Donor–acceptor (D–A) conjugated polymeric HTMs have recently shown remarkable performance in PSCs due to their strong push–pull effect<sup>24–27</sup> and multiple charge transfer pathways using both intermolecular (i.e., charge hopping) and intramolecular charge transfer (ICT).<sup>28,29</sup> However, an ideal HTM should have optimized molecular interactions to achieve both the film-forming ability and high charge mobility without dopants.<sup>30–32</sup> The conjugated D–A polymeric HTMs with strong molecular packing have high charge mobility, but excessive intermolecular interactions lower film-forming properties in perovskites, causing interfacial nonradiative recombination.<sup>30,33</sup> To optimize the molecular interaction, side chain engineering (e.g., extended, polar, and asymmetric

Received: January 27, 2023

Accepted: March 20, 2023

Published: March 21, 2023



ACS Publications

© 2023 American Chemical Society

1839

<https://doi.org/10.1021/acsenergylett.3c00211>  
*ACS Energy Lett.* 2023, 8, 1839–1847

side chains) has been employed as a representative effective strategy.<sup>34,35</sup> However, extending these substituents inevitably impairs the intermolecular  $\pi$ - $\pi$  stacking and decreases the charge hopping efficiency due to an increased energetic barrier for charge transport.<sup>36</sup>

In this study, the design of D-A conjugated polymeric HTMs (Asy-PSDTS and Asy-PSeDTS) employing unsubstituted rigid segments has been proposed to overcome these limitations and compare their performance with those of polymers without a rigid segment (Asy-PDTS) (Figure 1a).

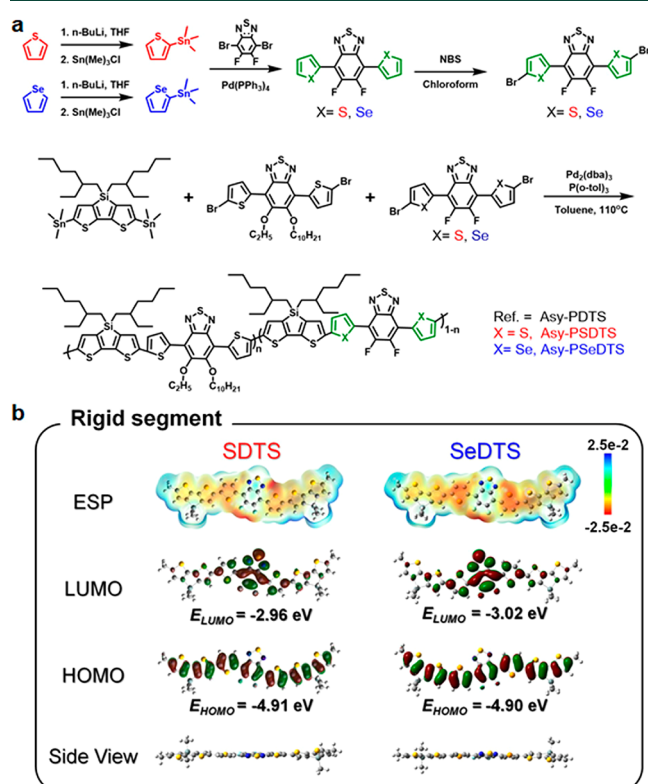


**Figure 1.** (a) Synthetic routes of the intermediate compounds and Asy-PDTS polymers (Asy-PDTS, Asy-PSDTS, and Asy-PSeDTS). (b) DFT calculations performed at the B3LYP/6-31G(d,p) level of rigid segment: SDTS and SeDTS (theoretical ESP, molecular orbital distribution, and side view of optimized molecular geometries).

Dithienosilole (DTS) is used as the donor unit, and an asymmetric alkyl substituent on the benzothiadiazole (BT) unit is adopted to modulate intermolecular interactions. A chalcogenide-based fluorinated BT is applied as a second rigid segment acceptor unit to generate an efficient charge hopping channel, compensating for the charge transport property. The rigid segment is constructed into planar structures of face-to-face stacking via chalcogenide–fluorine noncovalent interactions (S···F and Se···F) via a conformation-locking approach.<sup>37–39</sup> Particularly, the extended lone pair electrons on the selenium atom (Se) can take part in delocalized aromaticity, because the Se is more polarizable than the sulfur atom (S).<sup>37</sup> Therefore, Asy-PSeDTS can induce stronger intermolecular interactions than Asy-PSDTS, facilitating intermolecular charge transport. Consequently, the Asy-PSeDTS-based PQD-SCs achieved a 15.2% PCE, outperforming doped Spiro-OMeTAD-based PQD-SCs (14.0%). In addition, these polymeric HTMs significantly contributed to

phase stability by completely blocking the external environment and optimizing the interaction between molecules to completely cover the PQD surface.

The unencapsulated Asy-PSeDTS-based PQD-SCs maintained 80% of the initial PCE after 40 days in 25–35% relative humidity (RH), showing significantly improved stability compared with the completely degraded Spiro-OMeTAD-based PQD-SCs.

The synthetic routes of Asy-PDTS, Asy-PSDTS, and Asy-PSeDTS are shown in **Scheme S1**, and their detailed synthetic procedures and characterization data are provided in the **Supporting Information** (Figures S2–S11 and Table S1). To evaluate the chain conformation, the optical characteristics of Asy-PDTS, Asy-PSDTS, and Asy-PSeDTS were investigated (Figure S12). Their detailed absorption characteristics are summarized in **Table S1**. The energy levels of the polymers were measured using cyclic voltammetry (CV), and the highest occupied molecular orbital (HOMO) energy level was estimated from the CV's oxidation onset (Figure S13). Asy-PDTS, Asy-PSDTS, and Asy-PSeDTS exhibited HOMO values of −5.19, −5.28, and −5.29 eV, respectively. From the HOMO energy levels and  $E_g$ , the lowest unoccupied molecular orbital (LUMO) energy levels were calculated as −3.33, −3.40, and −3.41 eV, respectively. The thermal stability of each polymer was evaluated by thermal gravimetric analysis under a N<sub>2</sub> atmosphere. The temperature for 5% weight loss was 311 °C, providing sufficient thermal stability during device fabrication (Figure S14). In addition, the effect of the rigid segment on the thermal properties was observed by differential scanning calorimetry (Figure S15). Asy-PDTS indicated weak melting ( $T_m$ ) and crystallization temperature ( $T_c$ ) peaks upon heating and cooling, whereas Asy-PSDTS and Asy-PSeDTS with rigid segments did not show an obvious phase transition.

DFT calculations were performed to investigate the impact of rigid segments with planar structures on the properties of Asy-PDTS, including the electrostatic surface potential (ESP), molecular orbital energy, and geometrical configuration of rigid segments (Figure 1b). The negative ESP (red) of both rigid segments was found to be mainly located on the fluorine of the BT monomer and localized on the S or Se that serves as a bridge. This negative charge could passivate the under-coordinated Pb<sup>2+</sup> on the PQD surface through Lewis-base passivation,<sup>40,41</sup> which enhances the interaction properties with PQDs, contributing to the charge transfer and phase stability. As shown in Figure 1b, in the calculations of the frontier molecular orbital energy levels, the two rigid segments have a nodal plane at the HOMO level, indicating that they are less affected by the HOMO level and have −4.91 eV, respectively. The LUMO level is relatively delocalized, showing that SeDTS (−3.02 eV) has a slightly lower LUMO level than that of SDTS (−2.96 eV).

Furthermore, the side view shows that their geometry is fixed by the chalcogen–halide noncovalent interaction between the core BT monomers and bridge, indicating that the rigid segments with an enhanced coplanar structure can work as molecular interjunctions that facilitate efficient intermolecular charge transport.

To further investigate the planarity of the rigid segments, relaxed potential energy scans (PESs) were calculated by varying the dihedral angle between the DTS and the bridge (i.e., thiophene and selenophene) unit. The SeDTS-based rigid segment had a higher  $\cos^2\varphi$  value (a planarity index)<sup>42</sup> than the SDTS-based rigid segment (Figure 2a), suggesting that

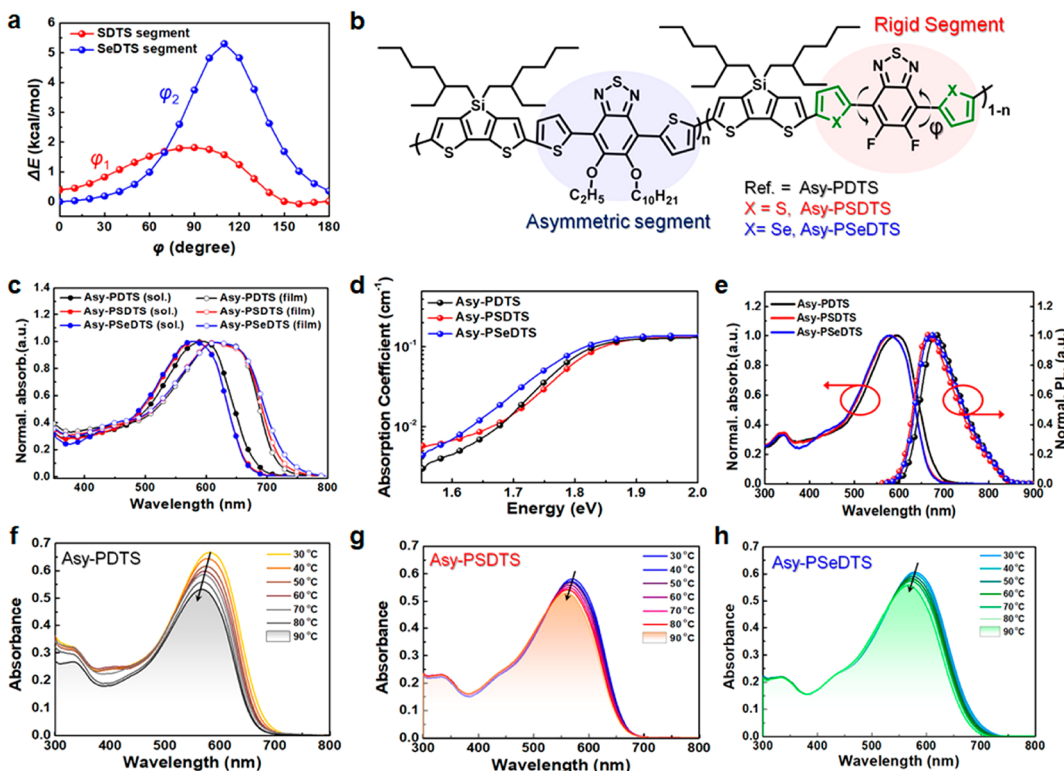


**Figure 2.** (a) PES results of torsional angles in Asy-PSDTS and Asy-PSeDTS. (b) Chemical structures of Asy-PDTS, Asy-PSDTS, and Asy-PSeDTS. (c) Normalized UV–vis absorption spectra of Asy-PDTS, Asy-PSDTS, and Asy-PSeDTS in CB solutions and film state. (d) Absorption coefficients of polymer films measured by PDS. (e) Normalized absorption (solid lines) and PL spectra (lines with symbols) and the temperature-dependent UV–vis absorption for (f) Asy-PDTS, (g) Asy-PSDTS, and (h) Asy-PSeDTS in CB with  $2.0 \times 10^{-5}$  M.

SeDTS has a strong planarization tendency due to a significantly higher torsional barrier than SDTS (Figure 2b).

We used ultraviolet–visible (UV–vis) spectroscopy to investigate the optical properties and the microscopic morphological behavior of the three HTMs. Each polymeric HTM exhibited a red-shift in the absorption maximum ( $\lambda_{\max}$ ) (Figure 2c). Particularly, Asy-PSDTS and Asy-PSeDTS, which had rigid segments, showed more red-shifts and broader absorption tails, suggesting that the rigid segment promotes strong  $\pi$ – $\pi$  stacking of the polymer backbone. Meanwhile, the broader absorption tail reflects the torsional disorder of the polymer backbone or the morphology of the semiconducting polymer film.<sup>43</sup> Therefore, to evaluate the structural disorder of the HTMs, we measured their Urbach energies ( $E_U$ ) using the photothermal deflection spectroscopy (PDS) technique (Figure 2d)

$$\alpha = \alpha_0 \exp\left[\frac{h\nu - E_g}{E_U}\right] \quad (1)$$

where  $\alpha_0$  denotes the absorption coefficient,  $E_U$  represents the Urbach energy,  $h$  is Planck's constant, and  $\nu$  denotes the incident photon frequency.<sup>44</sup> Asy-PSDTS (61.1 meV) and Asy-PSeDTS (74.2 meV) exhibit larger Urbach energies than those of Asy-PDTS (59.8 meV). Moreover, as shown in Figure 2e, the Stokes shifts of Asy-PSDTS and Asy-PSeDTS are 98 and 106 nm, respectively, larger than those of Asy-PDTS (95 nm). Similarly, at the full width at half-maximum (fwhm), Asy-PSDTS and Asy-PSeDTS are larger (102.0 and 104.7 nm, respectively) than Asy-PDTS (99.1 nm). Previous reports have demonstrated that conjugated polymers with an increased

disorder exhibit larger Stokes shifts and fwhm of the emission peaks.<sup>43,45,46</sup> From the comprehensive results, we speculated that the rigid segment provides closer face-to-face stacking and inhibits polymer backbone crystallization during the phase transition from the solution state to the solid state, causing structural disorder. We observed temperature-dependent UV–vis spectra of the three HTMs to further clarify this interpretation. As the temperature increased, HTMs released their aggregation due to a reduction in intermolecular interactions. Comparing the polymeric HTMs, Asy-PDTS showed a high decrease in the 0–0 transition peak and a large blue shift (Figure 2f), whereas Asy-PSDTS and Asy-PSeDTS showed slight variations (Figure 2g and h). The difference implies that their polymer solutions exhibit a less ordered system due to the strong intermolecular interactions of rigid segments.

Atomic force microscopy (AFM) and two-dimensional grazing-incidence wide-angle X-ray scattering (2D-GIWAXS) were performed to investigate the retention of the solution-phase polymer behavior by the rigid segment in the solid film state. As illustrated in the AFM images (Figure S16), the root-mean-square roughness values are 1.16, 0.81, and 0.55 nm for Asy-PDTS, Asy-PSDTS, and Asy-PSeDTS, respectively. By suppressing crystallization, the polymer films with a rigid segment exhibited smoother morphologies than Asy-PDTS, which is advantageous for the complete coverage of the PQD surface and can minimize current leakage. To compare the micromorphology of polymer films, 2D-GIWAXS analysis was performed upon thermal annealing (TA) at different temperatures. The resulting 2D-GIWAXS patterns and corresponding line-cut profiles in the out-of-plane (OOP) and in-plane are

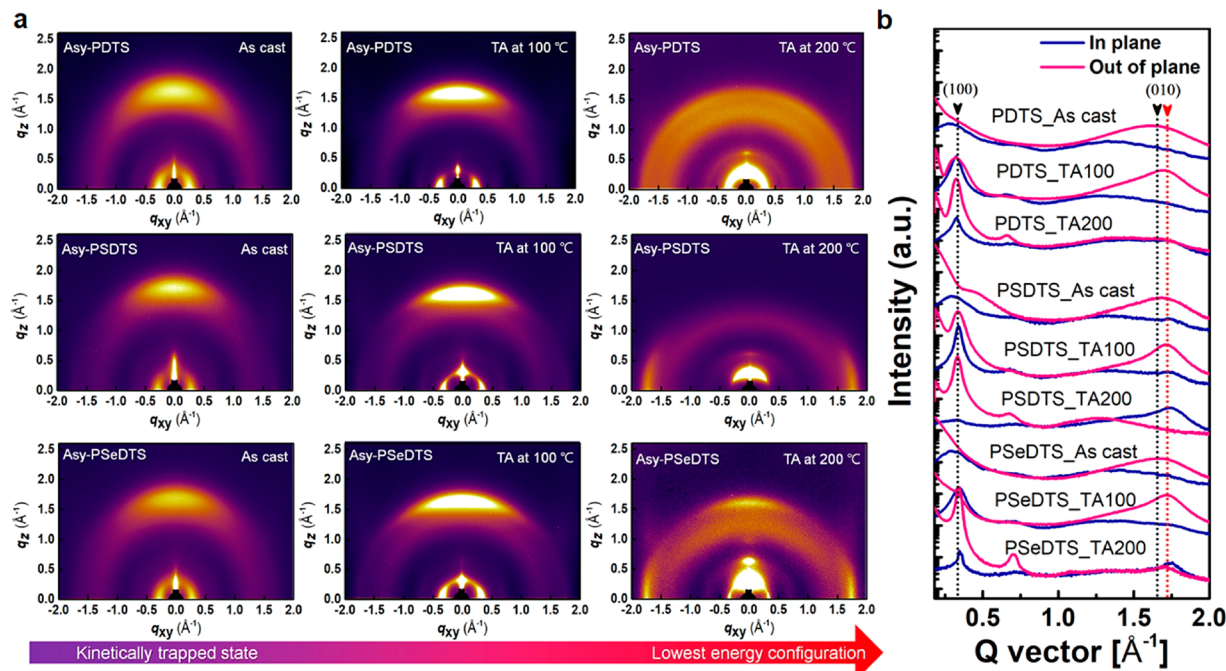


**Figure 3.** (a) 2D-GIWAXS patterns of Asy-PDTs, Asy-PSDTS, and Asy-PSeDTS. (b) Scattering profiles at different TA temperatures (black line,  $\pi-\pi$  stacking of Asy-PDTs; red line,  $\pi-\pi$  stacking of Asy-PSDTS and Asy-PSeDTS).

shown in Figure 3. The crystallographic information about the three HTMs is summarized in Table S2, and it was found that all HTMs exhibited face-on orientations before TA treatment. Using the Scherrer equation, the crystal coherence lengths ( $L_{100}$ ) of the polymers were calculated to be 37.6 (Asy-PDTs), 34.2 (Asy-PSDTS), and 32.5 Å (Asy-PSeDTS) at the lamellar peak. Although Asy-PSDTS and Asy-PSeDTS showed relatively lower crystallinity than Asy-PDTs in the as-cast state, their  $\pi-\pi$  stacking distances ( $d_{010}$ ) along the OOP direction were 3.76 and 3.71 Å, respectively, which were significantly closer than that of Asy-PDTs (3.93 Å). In addition, TA was performed to explore morphological change with increasing mobility of the polymer chain. The TA promotes the segmental chain motion of the polymers, yielding an ordered crystalline structure. After 100 °C TA of the polymers, their 2D-GIWAXS peaks became narrower and stronger. However, Zhao et al.<sup>47</sup> recently demonstrated that, as the degree of thermal motion increases, the lattice vibrations of the crystalline domain increase, triggering  $\pi-\pi$  stacking to destroy the packed structures. After 200 °C TA, Asy-PDTs showed an amorphous morphology with the face-on domain totally collapsed. Meanwhile, Asy-PSDTS and Asy-PSeDTS were also rearranged to edge-on and bimodal orientations, respectively, but they maintained their  $\pi-\pi$  stacking and intermolecular interaction. This edge-on transition align with the literature-reported tendency to generate strong edge-on orientations at lower side chain densities due to tighter packing between lamellas.<sup>48,49</sup> Notably, Asy-PSeDTS sustained face-on orientation even after 200 °C TA, attributable to relatively robust  $\pi-\pi$  stacking compared to the SDTS rigid segment.

The charge transfer benefits crystalline regions through ICT but is limited to amorphous regions. The rigid segments decrease polymer crystallinity but improve closed  $\pi-\pi$  stacking, which enhances charge hopping efficiency (Figure S17). To determine the enhancement of charge transport, we performed space-charge-limited current (SCLC) measure-

ments to obtain the hole mobility ( $\mu_h$ ) of the three polymers (Figure 4a). The  $\mu_h$  of Asy-PSDTS ( $7.18 \times 10^{-4} \text{ cm}^2 \text{ V}^{-1} \text{ s}^{-1}$ ) and Asy-PSeDTS ( $9.17 \times 10^{-4} \text{ cm}^2 \text{ V}^{-1} \text{ s}^{-1}$ ) was significantly improved compared to that of Asy-PDTs ( $2.87 \times 10^{-4} \text{ cm}^2 \text{ V}^{-1} \text{ s}^{-1}$ ). We also compared the conductivity of three polymers (Figure S18) and found that Asy-PSeDTS had the highest conductivity ( $8.79 \times 10^{-5} \text{ S cm}^{-1}$ ), followed by Asy-PSDTS ( $5.81 \times 10^{-5} \text{ S cm}^{-1}$ ) and Asy-PDTs ( $4.32 \times 10^{-5} \text{ S cm}^{-1}$ ). These results can be explained by the relatively improved intermolecular charge transport ability induced by rigid segments,<sup>25</sup> consistent with the GIWAXS results (Figure 3).

To verify the hole extraction property, we performed time-resolved photoluminescence (PL) decay traces and steady-state PL spectra measurements on bilayer films (glass/CsPbI<sub>3</sub> PQDs/HTM). Figure 4b shows the time-resolved PL decay curves of each sample fitted with a two-component exponential decay model. The PL lifetimes were 28.0, 8.34, 1.98, and 1.69 ns for the bare PQD and Asy-PDTs-, Asy-PSDTS-, and Asy-PSeDTS-based films, respectively. This result indicates Asy-PSeDTS exhibited the best hole extraction capability among the three HTMs. Figure 4c shows the steady-state PL spectra of each sample. The highest PL quenching efficiency is observed in Asy-PSeDTS-based film, indicating that more charge carriers contribute to photocurrent.<sup>50,51</sup> Asy-PSeDTS-based film also exhibited a greater blue-shift of PL spectra than Asy-PDTs- and Asy-PSDTS-based films (inset image), revealing decreased trap states and better passivation of the PQD layer.<sup>52,53</sup>

To investigate the interaction between the HTMs and the PQD surface, we built PQD slabs and calculated the adsorption behavior of the HTM rigid segments (Figure S19). Two rigid segments (SDTS and SeDTS) of HTMs were positioned above a PQD crystal model, and subsequent limitations were optimized for the (001) surface with CsI termination. We then calculated the adsorption energies ( $E_{\text{ads}}$ ) of the rigid segments on the PQD surface (Figure 4d), using

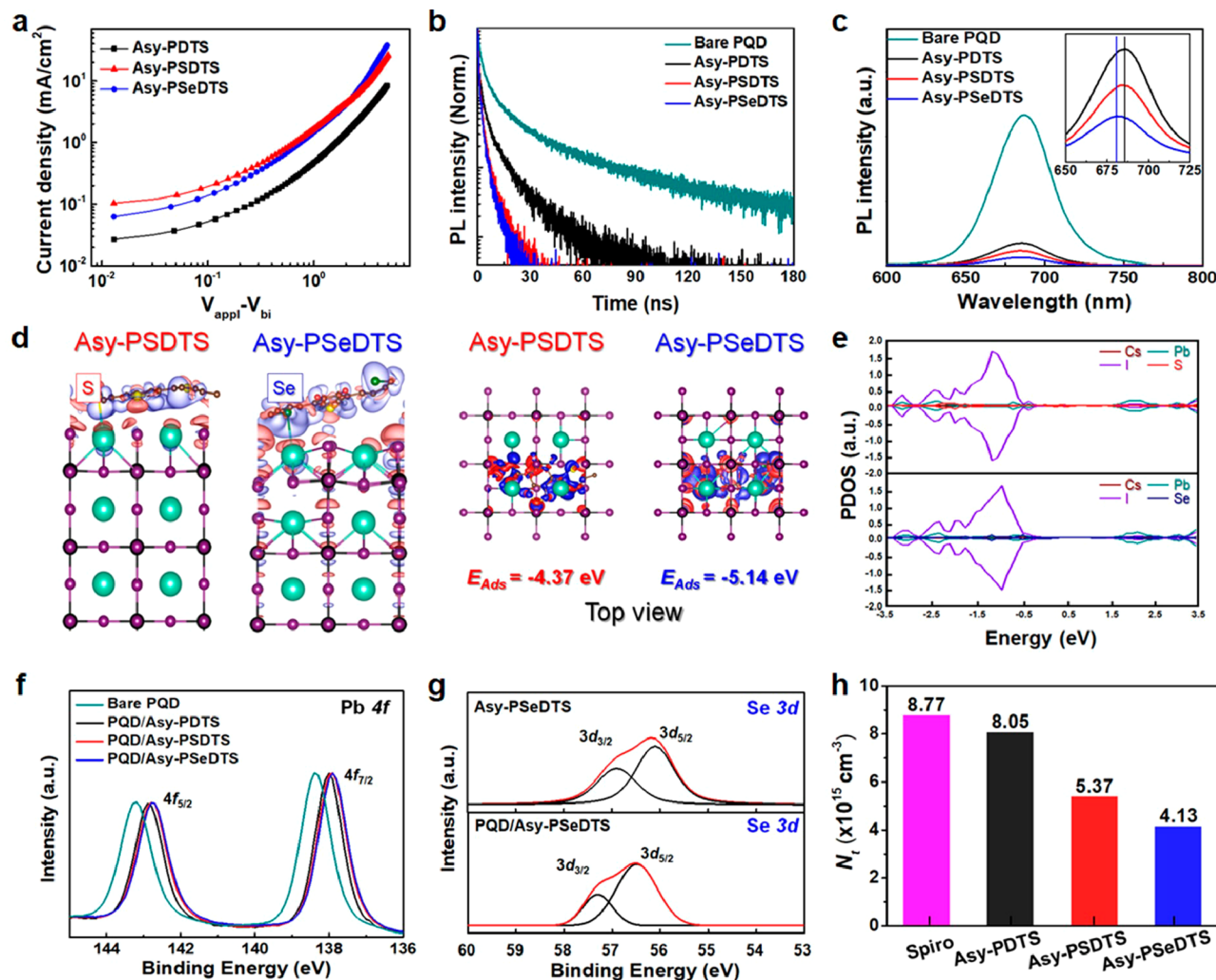


**Figure 4.** (a) Hole mobility of neat Asy-PDTS, Asy-PSDTS, and Asy-PSeDTs films. (b) Time-resolved PL decay curves of bare and three dopant-free HTM-based PQD films. (c) Steady-state PL spectra of bare and three dopant-free HTMs-based PQD films; the inset represents a zoom-in of PL spectra. (d) Theoretical interaction behavior of rigid segments of HTMs on a CsPbI<sub>3</sub> PQD surface. (e) The projected density of state profiles for the optimum adsorption configuration of each rigid segment on the CsPbI<sub>3</sub> PQD surface. XPS spectra of (f) Pb 4f and (g) Se 3d of bare and polymeric HTM-coated CsPbI<sub>3</sub> PQD films. (h) Trap state densities of different HTM-based PQD films.

the equation  $E_{\text{Ads}} = E_{\text{total}} - E_{\text{slab}} - E_{\text{rigid segment}}$ . The SeDTs segment exhibited a significantly higher binding energy than the SDTS segment. This strong interaction is also identified in the defect system of iodine vacancies (Figure S20). Furthermore, the trap-density at the n-type level is effectively alleviated in the SeDTs system (Figure S21). These results suggest a more robust packing between Asy-PSeDTs and PQDs, which can contribute to efficient hole extraction and defect passivation (Figure 4e).

To experimentally evaluate the chemical interaction between the rigid segment and PQDs, X-ray photoelectron spectroscopy (XPS) measurements were performed. Compared with the pristine PQD film, HTM-coated PQD films exhibited shifts in the Pb 4f peaks toward lower binding energy (Figure 4f), indicating changed chemical conditions around Pb<sup>2+</sup> on the PQD surface. The negative shift of the Pb 4f peaks increased from Asy-PDTS to Asy-PSDTS and Asy-PSeDTs, indicating the strongest interaction between Asy-PSeDTs and PQDs.<sup>24</sup> The Se 3d peaks showed shifts toward higher binding energies from Asy-PSeDTs to PQD/Asy-PSeDTs (Figure 4g), indicating a direct interaction between Se in Asy-PSeDTs

and the PQD surface and suggesting efficient defect passivation.<sup>25</sup> Further, we performed SCLC measurements and estimated the trap state densities ( $N_t$ ) of each HTM-based device (Figure S22 and Figure 4h). Asy-PSeDTs-coated PQD films showed the most reduced trap-densities, demonstrating efficient defect passivation at the PQD/Asy-SeDTs interface.

We fabricated n-i-p-type PQD-SCs with the device configuration of FTO/TiO<sub>2</sub>/CsPbI<sub>3</sub> PQDs/HTM/MoO<sub>x</sub>/Ag and compared their photovoltaic performances (Figure 5a). The energy levels of each polymeric HTM are suitable for blocking electrons and extracting holes. The  $J-V$  curves of champion PQD-SCs based on dopant-free HTMs and doped Spiro-OMeTAD are shown in Figure 5b, and their photovoltaic parameters are recorded in Table S3. The Asy-PSeDTs-based device recorded a PCE of 15.2%, higher than that of the doped Spiro-OMeTAD-based device (14.0%). The high reproducibility of PQD-SCs comprising Spiro-OMeTAD and Asy-PSeDTs is investigated statistically for all photovoltaic parameters (Figure S23). These results suggest that the dopant-free polymer can sufficiently replace Spiro-OMeTAD as the HTM of PQD-SCs.

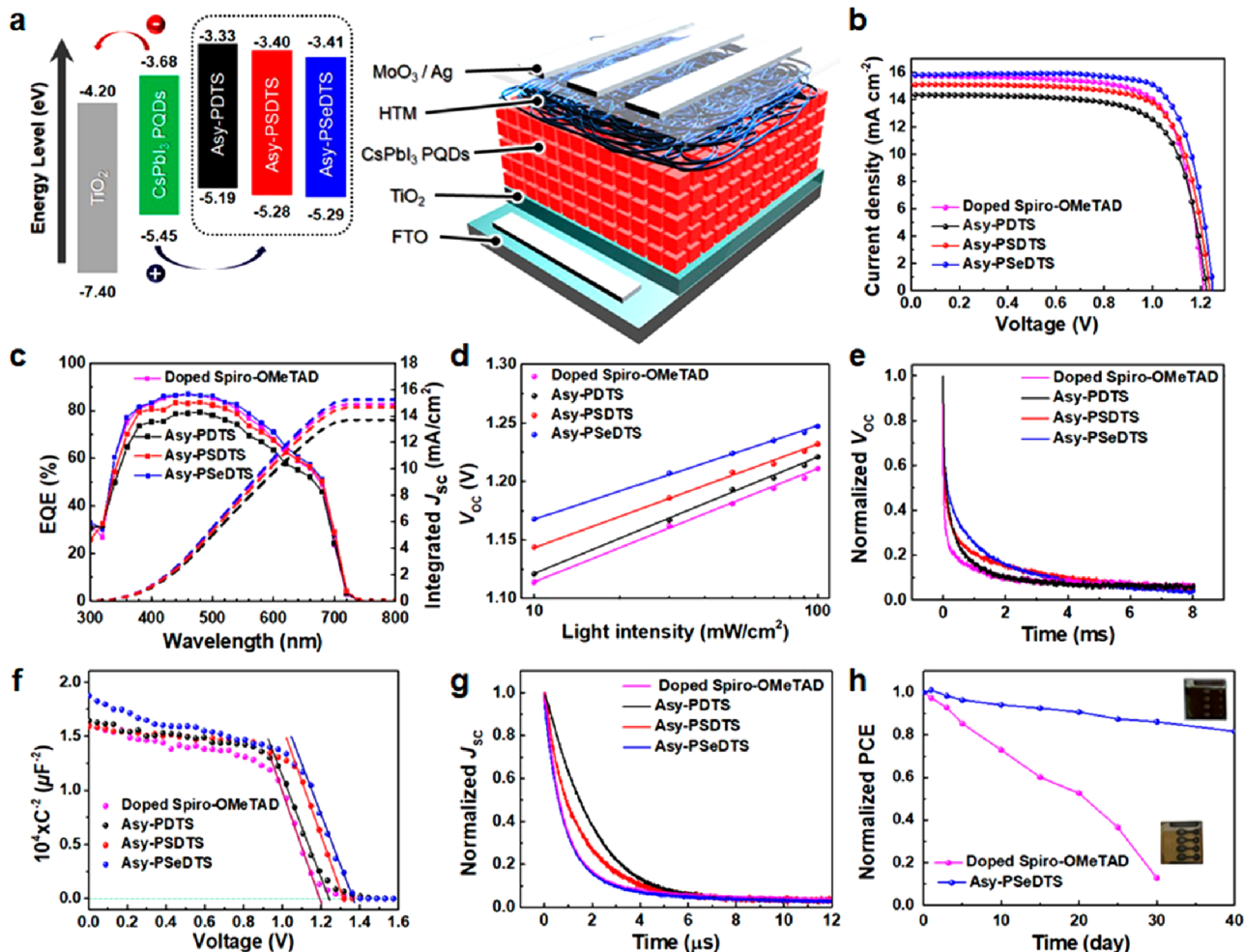


**Figure 5.** (a) Energy level alignment of  $\text{CsPbI}_3$  PQDs and three HTMs in the device architecture of FTO/TiO<sub>2</sub>/CsPbI<sub>3</sub> PQDs/HTM/MoO<sub>3</sub>/Ag. (b) Current density–voltage curves and (c) EQE spectra and integrated  $J_{\text{SC}}$  of the best-performing PQD-SCs. (d) Light-intensity-dependent  $V_{\text{OC}}$ , (e) Mott–Schottky plots, (f) normalized transient photovoltage, and (g) transient photocurrent of the doped Spiro-OMeTAD-based and three HTM-based devices. (h) Stability tests of PQD-SCs comprising doped Spiro-OMeTAD and Asy-PSeDTS under the 25–35% RH condition.

In addition, all photovoltaic parameters show a stepwise increase from Asy-PDTS to Asy-PSeDTS. We interpret this result as follows: (1) The deep HOMO level of Asy-PSeDTS can influence the quasi-Fermi level to improve the  $V_{\text{OC}}$ . (2) The rigid segment of Asy-PSeDTS passivates the PQD surface and facilitates interface charge separation, resulting in better  $V_{\text{OC}}$  and  $J_{\text{SC}}$ . (3) The high  $\mu_{\text{h}}$  and conductivity of Asy-PSeDTS can reduce the series resistance and improve  $J_{\text{SC}}$  and FF. Figure S24 presents that the Asy-PSeDTS-based devices exhibited a smaller hysteresis index than the doped Spiro-OMeTAD-based devices, indicating that polymeric HTM can enhance balanced charge carrier transport within PQD-SCs. In addition, the operation stability of the polymeric HTM-based PQD-SCs was demonstrated through maximum power point tracking (Figure S25). The external quantum efficiency (EQE) spectra of each HTM-based device are presented in Figure 5c. The fully integrated  $J_{\text{SC}}$  values are 13.7 (Asy-PDTS), 14.6 (Asy-PSCTS), and 15.2 mA cm<sup>-2</sup> (Asy-PSeDTS). These values well match the  $J_{\text{SC}}$  values obtained from the  $J$ – $V$  curve.

To identify the cause of the improved performance of Asy-PSeDTS-based PQD-SCs, the charge carrier dynamics was analyzed. Through light-intensity-dependent  $V_{\text{OC}}$  measurements, we compared the ideal factor (slope) of each HTM-

based device (Figure 5d). The slope was the highest in the doped Spiro-OMeTAD-based device ( $1.79 \text{ } kT/q$ ) and decreased sequentially to 1.67, 1.48, and  $1.32 \text{ } kT/q$  for the Asy-PDTS-, Asy-PSCTS-, and Asy-PSeDTS-based devices, respectively. This tendency indicates that trap-assisted recombination is most efficiently suppressed in the Asy-PSeDTS-based device. In addition, reduced charge recombination was demonstrated by transient photovoltage measurements (Figure 5e), where the Asy-PSeDTS-based device exhibited the longest lifetime. To understand the effect of reduced trap-assisted recombination on the charge extraction properties, we performed the capacitance–voltage ( $C^{-2}-V$ ) measurement of each HTM-based device (Figure 5f). The Asy-PSeDTS-based device exhibits a built-in potential ( $V_{\text{bi}}$ ) of 1.36 V, significantly higher than those of doped Spiro-OMeTAD (1.19 V), Asy-PDTS (1.23 V), and Asy-PSCTS-based devices (1.31 V). The highest  $V_{\text{bi}}$  of Asy-PSeDTS agrees with the  $V_{\text{OC}}$  and FF trends obtained from the  $J$ – $V$  curves, suggesting that the depletion region expansion contributed to improved device efficiency. The efficient charge carrier extraction ability of Asy-PSeDTS is further demonstrated by the shortest charge extraction time in transient photocurrent measurements (Figure 5g).

Moisture-induced  $\alpha$ -phase degradation of PQDs is a critical issue in PQD-SCs.<sup>4,8,9</sup> We determined the effect of the dopant-free polymeric HTM on the overall device stability (Figure S<sub>h</sub>). The unencapsulated Asy-PSeDTS and doped Spiro-OMeTAD devices were stored under ambient conditions (RH = 25–35%). After 30 days, the PCE of the doped Spiro-OMeTAD-based device retained only 13% of its initial PCE. The lithium salt doped in Spiro-OMeTAD adsorbs H<sub>2</sub>O from the air, degrading the underlying PQD layer. In contrast, the Asy-PSeDTS-based device retained 80% of its initial PCE after 40 days. Asy-PSeDTS is hydrophobic with a higher contact angle than that of doped Spiro-OMeTAD (Figure S<sub>26</sub>), and the PQD/HTM passivation results explain its improved stability.

In summary, we designed three D–A conjugated polymeric HTMs: Asy-PDTS, Asy-PSDTS, and Asy-PSeDTS. The copolymers were evaluated in photovoltaics to investigate the impact of rigid segments on charge transport and intermolecular interaction. Asy-PSeDTS, with high polarizability, exhibited stronger conformation-locking effects than Asy-PSDTS, leading to a better charge transport performance. The Asy-PSeDTS-based device showed an excellent PCE of 15.2%, the highest reported among dopant-free HTM-based PQD-SCs (Table S4). Moreover, the Asy-PSeDTS-based device maintained 80% of its initial PCE under ambient conditions (RH = 25–35%) without encapsulation for 40 days. Our results demonstrate the effectiveness of rigid segment-based dopant-free HTMs in achieving high-performance PQD-SCs.

## ■ ASSOCIATED CONTENT

### SI Supporting Information

The Supporting Information is available free of charge at <https://pubs.acs.org/doi/10.1021/acsenergylett.3c00211>.

Experimental details, material synthesis, GPC, <sup>1</sup>H NMR, <sup>13</sup>C NMR, and MALDI-TOF MS data, UV-vis absorption spectra, PL emission spectra, CV, TGA curve, DSC thermograms, AFM, conductivity, theoretical calculation, SCLC measurement, device histograms, device hysteresis curves, stabilized power output and stability measurement, water droplet contact angle, crystallographic information, and photovoltaic parameter (PDF)

## ■ AUTHOR INFORMATION

### Corresponding Authors

Sung Beom Cho – Department of Materials Science & Engineering and Department of Energy Systems Research, Ajou University, Suwon 16499, Republic of Korea;  
Email: [csb@ajou.ac.kr](mailto:csb@ajou.ac.kr)

Hong Il Kim – Department of Chemical Engineering, Pohang University of Science and Technology (POSTECH), Pohang, Gyeongbuk 37673, Korea; Email: [hongilkim@postech.ac.kr](mailto:hongilkim@postech.ac.kr)

Taiho Park – Department of Chemical Engineering, Pohang University of Science and Technology (POSTECH), Pohang, Gyeongbuk 37673, Korea; [orcid.org/0000-0002-5867-4679](https://orcid.org/0000-0002-5867-4679); Email: [taihopark@postech.ac.kr](mailto:taihopark@postech.ac.kr)

### Authors

Dae Hwan Lee – Department of Chemical Engineering, Pohang University of Science and Technology (POSTECH), Pohang, Gyeongbuk 37673, Korea

Seyeong Lim – Department of Chemical Engineering, Pohang University of Science and Technology (POSTECH), Pohang, Gyeongbuk 37673, Korea

Chanhyeok Kim – Department of Chemical Engineering, Pohang University of Science and Technology (POSTECH), Pohang, Gyeongbuk 37673, Korea

Han Uk Lee – Department of Materials Science & Engineering and Department of Energy Systems Research, Ajou University, Suwon 16499, Republic of Korea

Dasol Chung – Department of Chemical Engineering, Pohang University of Science and Technology (POSTECH), Pohang, Gyeongbuk 37673, Korea

Yelim Choi – Department of Chemical Engineering, Pohang University of Science and Technology (POSTECH), Pohang, Gyeongbuk 37673, Korea

Jongmin Choi – Department of Energy Science and Engineering, Daegu Gyeongbuk Institute of Science and Technology (DGIST), Daegu 42988, Republic of Korea;  
[orcid.org/0000-0001-8904-0946](https://orcid.org/0000-0001-8904-0946)

Younghoon Kim – Department of Chemistry, Kookmin University, Seoul 02707, Republic of Korea; [orcid.org/0000-0002-0773-2146](https://orcid.org/0000-0002-0773-2146)

Complete contact information is available at:  
<https://pubs.acs.org/10.1021/acsenergylett.3c00211>

### Author Contributions

<sup>#</sup>D.H.L., S.L.: These authors contributed equally to this work.

### Notes

The authors declare no competing financial interest.

## ■ ACKNOWLEDGMENTS

2D-GIWAXD measurements were performed at a synchrotron radiation on the 9A beamline at the Pohang Accelerator Laboratory (PAL), Korea. This work was supported by National Research Foundation of Korea (NRF) grants funded by Ministry of Science and ICT (MSIT) (No. 2021R1A2C3004420, 2022M3J1A1064317, 2021R1A5A1084921) and the NRF of Korea grant funded by the Korean Government (NRF-2019-Global Ph.D. Fellowship Program). The computational resources were supported by Korea Supercomputing Center (KSC-2022-CRE-0042).

## ■ REFERENCES

- (1) Chen, H.; Pina, J. M.; Hou, Y.; Sargent, E. H. Synthesis, Applications, and Prospects of Quantum-Dot-in-Perovskite Solids. *Adv. Energy Mater.* **2022**, *12* (4), 2100774.
- (2) Chen, J.; Jia, D.; Johansson, E. M. J.; Hagfeldt, A.; Zhang, X. Emerging perovskite quantum dot solar cells: feasible approaches to boost performance. *Energy Environ. Sci.* **2021**, *14* (1), 224–261.
- (3) Chi, W.; Banerjee, S. K. Application of Perovskite Quantum Dots as an Absorber in Perovskite Solar Cells. *Angew. Chem., Int. Ed. Engl.* **2022**, *61* (9), e202112412.
- (4) Lim, S.; Lee, G.; Han, S.; Kim, J.; Yun, S.; Lim, J.; Pu, Y.-J.; Ko, M. J.; Park, T.; Choi, J.; et al. Monodisperse Perovskite Colloidal Quantum Dots Enable High-Efficiency Photovoltaics. *ACS Energy Lett.* **2021**, *6* (6), 2229–2237.
- (5) Liu, L.; Najar, A.; Wang, K.; Du, M.; Liu, S. F. Perovskite Quantum Dots in Solar Cells. *Adv. Sci.* **2022**, *9* (7), 2104577.
- (6) Dias, J. A.; Santagneli, S. H.; Ribeiro, S. J. L.; Messadeg, Y. Perovskite Quantum Dot Solar Cells: An Overview of the Current Advances and Future Perspectives. *Sol. RRL* **2021**, *5* (8), 2100205.
- (7) Duan, L.; Hu, L.; Guan, X.; Lin, C. H.; Chu, D.; Huang, S.; Liu, X.; Yuan, J.; Wu, T. Quantum Dots for Photovoltaics: A Tale of Two Materials. *Adv. Energy Mater.* **2021**, *11* (20), 2100354.

- (8) Lim, S.; Han, S.; Kim, D.; Min, J.; Choi, J.; Park, T. Key Factors Affecting the Stability of CsPbI<sub>3</sub> Perovskite Quantum Dot Solar Cells: A Comprehensive Review. *Adv. Mater.* **2023**, *35*, 2203430.
- (9) Lim, S.; Kim, J.; Park, J. Y.; Min, J.; Yun, S.; Park, T.; Kim, Y.; Choi, J. Suppressed Degradation and Enhanced Performance of CsPbI<sub>3</sub> Perovskite Quantum Dot Solar Cells via Engineering of Electron Transport Layers. *ACS Appl. Mater. Interfaces* **2021**, *13* (5), 6119–6129.
- (10) Lim, S.; Lee, D. H.; Choi, H.; Choi, Y.; Lee, D. G.; Cho, S. B.; Ko, S.; Choi, J.; Kim, Y.; Park, T. High-Performance Perovskite Quantum Dot Solar Cells Enabled by Incorporation with Dimensionally Engineered Organic Semiconductor. *Nanomicro Lett.* **2022**, *14* (1), 204.
- (11) Wang, Q.; Jin, Z.; Chen, D.; Bai, D.; Bian, H.; Sun, J.; Zhu, G.; Wang, G.; Liu, S. F.  $\mu$ -Graphene Crosslinked CsPbI<sub>3</sub> Quantum Dots for High Efficiency Solar Cells with Much Improved Stability. *Adv. Energy Mater.* **2018**, *8* (22), 1800007.
- (12) Jia, D.; Chen, J.; Mei, X.; Fan, W.; Luo, S.; Yu, M.; Liu, J.; Zhang, X. Surface matrix curing of inorganic CsPbI<sub>3</sub> perovskite quantum dots for solar cells with efficiency over 16%. *Energy Environ. Sci.* **2021**, *14* (8), 4599–4609.
- (13) Jia, D.; Chen, J.; Qiu, J.; Ma, H.; Yu, M.; Liu, J.; Zhang, X. Tailoring solvent-mediated ligand exchange for CsPbI<sub>3</sub> perovskite quantum dot solar cells with efficiency exceeding 16.5%. *Joule* **2022**, *6* (7), 1632–1653.
- (14) Jia, D.; Chen, J.; Zhuang, R.; Hua, Y.; Zhang, X. Inhibiting lattice distortion of CsPbI<sub>3</sub> perovskite quantum dots for solar cells with efficiency over 16.6%. *Energy Environ. Sci.* **2022**, *15* (10), 4201–4212.
- (15) Shi, Y.; Yuan, L.; Liu, Z.; Lu, Y.; Yuan, B.; Shen, W.; Xue, B.; Zhang, Y.; Qian, Y.; Li, F.; et al. In Situ Growth of Strained Matrix on CsPbI(3) Perovskite Quantum Dots for Balanced Conductivity and Stability. *ACS Nano* **2022**, *16* (7), 10534–10544.
- (16) Zhang, L.; Kang, C.; Zhang, G.; Pan, Z.; Huang, Z.; Xu, S.; Rao, H.; Liu, H.; Wu, S.; Wu, X.; et al. All-Inorganic CsPbI<sub>3</sub> Quantum Dot Solar Cells with Efficiency over 16% by Defect Control. *Adv. Funct. Mater.* **2021**, *31* (4), 2005930.
- (17) Zhao, Q.; Hazarika, A.; Chen, X.; Harvey, S. P.; Larson, B. W.; Teeter, G. R.; Liu, J.; Song, T.; Xiao, C.; Shaw, L.; et al. High efficiency perovskite quantum dot solar cells with charge separating heterostructure. *Nat. Commun.* **2019**, *10* (1), 2842.
- (18) Ji, K.; Yuan, J.; Li, F.; Shi, Y.; Ling, X.; Zhang, X.; Zhang, Y.; Lu, H.; Yuan, J.; Ma, W. High-efficiency perovskite quantum dot solar cells benefiting from a conjugated polymer-quantum dot bulk heterojunction connecting layer. *J. Mater. Chem. A* **2020**, *8* (16), 8104–8112.
- (19) Yuan, J.; Zhang, X.; Sun, J.; Patterson, R.; Yao, H.; Xue, D.; Wang, Y.; Ji, K.; Hu, L.; Huang, S.; et al. Hybrid Perovskite Quantum Dot/Non-Fullerene Molecule Solar Cells with Efficiency Over 15%. *Adv. Funct. Mater.* **2021**, *31* (27), 2101272.
- (20) Zhang, X.; Huang, H.; Ling, X.; Sun, J.; Jiang, X.; Wang, Y.; Xue, D.; Huang, L.; Chi, L.; Yuan, J.; et al. Homojunction Perovskite Quantum Dot Solar Cells with over 1 microm-Thick Photoactive Layer. *Adv. Mater.* **2022**, *34* (2), 2105977.
- (21) Abate, A.; Leijtens, T.; Pathak, S.; Teuscher, J.; Avolio, R.; Errico, M. E.; Kirkpatrick, J.; Ball, J. M.; Docampo, P.; McPherson, I.; et al. Lithium salts as "redox active" p-type dopants for organic semiconductors and their impact in solid-state dye-sensitized solar cells. *Phys. Chem. Chem. Phys.* **2013**, *15* (7), 2572–2579.
- (22) Hawash, Z.; Ono, L. K.; Qi, Y. Recent Advances in Spiro-MeOTAD Hole Transport Material and Its Applications in Organic–Inorganic Halide Perovskite Solar Cells. *Adv. Mater. Interfaces* **2018**, *5* (1), 1700623.
- (23) Yuan, J.; Ling, X.; Yang, D.; Li, F.; Zhou, S.; Shi, J.; Qian, Y.; Hu, J.; Sun, Y.; Yang, Y.; et al. Band-Aligned Polymeric Hole Transport Materials for Extremely Low Energy Loss  $\alpha$ -CsPbI<sub>3</sub> Perovskite Nanocrystal Solar Cells. *Joule* **2018**, *2* (11), 2450–2463.
- (24) Fu, Q.; Liu, H.; Li, S.; Zhou, T.; Chen, M.; Yang, Y.; Wang, J.; Wang, R.; Chen, Y.; Liu, Y. Management of Donor and Acceptor Building Blocks in Dopant-Free Polymer Hole Transport Materials for High-Performance Perovskite Solar Cells. *Angew. Chem., Int. Ed. Engl.* **2022**, *61* (43), e202210356.
- (25) Fu, Q.; Tang, X.; Liu, H.; Wang, R.; Liu, T.; Wu, Z.; Woo, H. Y.; Zhou, T.; Wan, X.; Chen, Y.; et al. Ionic Dopant-Free Polymer Alloy Hole Transport Materials for High-Performance Perovskite Solar Cells. *J. Am. Chem. Soc.* **2022**, *144* (21), 9500–9509.
- (26) Lee, D. H.; Kim, D. H.; Kim, T.; Lee, D. C.; Cho, S.; Park, T. Solid-solvent hybrid additive for the simultaneous control of the macro- and micro-morphology in non-fullerene-based organic solar cells. *Nano Energy* **2022**, *93*, 106878.
- (27) Wu, B.; Fu, Q.; Sun, L.; Liu, Y.; Sun, Z.; Xue, S.; Liu, Y.; Liang, M. Conjugation Engineering of Spiro-Based Hole Transport Materials for Efficient and Stable Perovskite Solar Cells. *ACS Energy Lett.* **2022**, *7* (8), 2667–2676.
- (28) Li, Z. a.; Chueh, C.-C.; Jen, A. K. Y. Recent advances in molecular design of functional conjugated polymers for high-performance polymer solar cells. *Prog. Polym. Sci.* **2019**, *99*, 101175.
- (29) Xiao, J.; Xiao, Z.; Hu, J.; Gao, X.; Asim, M.; Pan, L.; Shi, C.; Zhang, X.; Zou, J.-J. Rational Design of Alkynyl-Based Linear Donor– $\pi$ –Acceptor Conjugated Polymers with Accelerated Exciton Dissociation for Photocatalysis. *Macromolecules* **2022**, *55* (13), 5412–5421.
- (30) Meng, D.; Xue, J.; Zhao, Y.; Zhang, E.; Zheng, R.; Yang, Y. Configurable Organic Charge Carriers toward Stable Perovskite Photovoltaics. *Chem. Rev.* **2022**, *122* (18), 14954–14986.
- (31) Yan, P.; Yang, D.; Wang, H.; Yang, S.; Ge, Z. Recent advances in dopant-free organic hole-transporting materials for efficient, stable and low-cost perovskite solar cells. *Energy Environ. Sci.* **2022**, *15* (9), 3630–3669.
- (32) Yin, X.; Song, Z.; Li, Z.; Tang, W. Toward ideal hole transport materials: a review on recent progress in dopant-free hole transport materials for fabricating efficient and stable perovskite solar cells. *Energy Environ. Sci.* **2020**, *13* (11), 4057–4086.
- (33) Wang, W.; Zhou, J.; Tang, W. Design of dopant-free small molecular hole transport materials for perovskite solar cells: a viewpoint from defect passivation. *J. Mater. Chem. A* **2022**, *10* (3), 1150–1178.
- (34) Lee, J.; Kim, G. W.; Kim, M.; Park, S. A.; Park, T. Nonaromatic Green-Solvent-Processable, Dopant-Free, and Lead-Capturable Hole Transport Polymers in Perovskite Solar Cells with High Efficiency. *Adv. Energy Mater.* **2020**, *10* (8), 1902662.
- (35) Lee, J.; Malekshahi Byranvand, M.; Kang, G.; Son, S. Y.; Song, S.; Kim, G. W.; Park, T. Green-Solvent-Processable, Dopant-Free Hole-Transporting Materials for Robust and Efficient Perovskite Solar Cells. *J. Am. Chem. Soc.* **2017**, *139* (35), 12175–12181.
- (36) Son, S. Y.; Kim, Y.; Lee, J.; Lee, G. Y.; Park, W. T.; Noh, Y. Y.; Park, C. E.; Park, T. High-Field-Effect Mobility of Low-Crystallinity Conjugated Polymers with Localized Aggregates. *J. Am. Chem. Soc.* **2016**, *138* (26), 8096–8103.
- (37) Fan, B.; Lin, F.; Wu, X.; Zhu, Z.; Jen, A. K. Selenium-Containing Organic Photovoltaic Materials. *Acc. Chem. Res.* **2021**, *S4* (20), 3906–3916.
- (38) Kim, H. G.; Kang, B.; Ko, H.; Lee, J.; Shin, J.; Cho, K. Synthetic Tailoring of Solid-State Order in Diketopyrrolopyrrole-Based Copolymers via Intramolecular Noncovalent Interactions. *Chem. Mater.* **2015**, *27* (3), 829–838.
- (39) Liu, D.; Kan, B.; Ke, X.; Zheng, N.; Xie, Z.; Lu, D.; Liu, Y. Extended Conjugation Length of Nonfullerene Acceptors with Improved Planarity via Noncovalent Interactions for High-Performance Organic Solar Cells. *Adv. Energy Mater.* **2018**, *8* (26), 1801618.
- (40) Bai, Y.; Hao, M.; Ding, S.; Chen, P.; Wang, L. Surface Chemistry Engineering of Perovskite Quantum Dots: Strategies, Applications, and Perspectives. *Adv. Mater.* **2022**, *34* (4), 2105958.
- (41) Choi, K.; Lee, D. H.; Jung, W.; Kim, S.; Kim, S. H.; Lee, D.; Song, S.; Park, T. 3D Interaction of Zwitterions for Highly Stable and Efficient Inorganic CsPbI<sub>3</sub> Solar Cells. *Adv. Funct. Mater.* **2022**, *32* (16), 2112027.

- (42) Che, Y.; Perepichka, D. F. Quantifying Planarity in the Design of Organic Electronic Materials. *Angew. Chem., Int. Ed. Engl.* **2021**, *60* (3), 1364–1373.
- (43) Wu, Y.; Schneider, S.; Walter, C.; Chowdhury, A. H.; Bahrami, B.; Wu, H. C.; Qiao, Q.; Toney, M. F.; Bao, Z. Fine-Tuning Semiconducting Polymer Self-Aggregation and Crystallinity Enables Optimal Morphology and High-Performance Printed All-Polymer Solar Cells. *J. Am. Chem. Soc.* **2020**, *142* (1), 392–406.
- (44) Zhang, C.; Mahadevan, S.; Yuan, J.; Ho, J. K. W.; Gao, Y.; Liu, W.; Zhong, H.; Yan, H.; Zou, Y.; Tsang, S.-W.; et al. Unraveling Urbach Tail Effects in High-Performance Organic Photovoltaics: Dynamic vs Static Disorder. *ACS Energy Lett.* **2022**, *7* (6), 1971–1979.
- (45) Kohler, A.; Hoffmann, S. T.; Bassler, H. An order-disorder transition in the conjugated polymer MEH-PPV. *J. Am. Chem. Soc.* **2012**, *134* (28), 11594–11601.
- (46) Yan, X.; Xiong, M.; Deng, X. Y.; Liu, K. K.; Li, J. T.; Wang, X. Q.; Zhang, S.; Prine, N.; Zhang, Z.; Huang, W.; et al. Approaching disorder-tolerant semiconducting polymers. *Nat. Commun.* **2021**, *12* (1), 5723.
- (47) Yang, L.; Wu, Y.; Yan, Y.; Wang, Z.; Qiao, Y.; Chang, D.; Zhang, C.; Wang, Y.; Lu, X.; Liu, Y.; et al. Molecular Packing and Charge Transport Behaviors of Semiconducting Polymers Over a Wide Temperature Range. *Adv. Funct. Mater.* **2022**, *32* (33), 2202456.
- (48) Liu, X.; He, B.; Garzón-Ruiz, A.; Navarro, A.; Chen, T. L.; Kolaczkowski, M. A.; Feng, S.; Zhang, L.; Anderson, C. A.; Chen, J.; et al. Unraveling the Main Chain and Side Chain Effects on Thin Film Morphology and Charge Transport in Quinoidal Conjugated Polymers. *Adv. Funct. Mater.* **2018**, *28* (31), 1801874.
- (49) Zhang, X.; Richter, L. J.; DeLongchamp, D. M.; Kline, R. J.; Hammond, M. R.; McCulloch, I.; Heeney, M.; Ashraf, R. S.; Smith, J. N.; Anthopoulos, T. D.; et al. Molecular packing of high-mobility diketo pyrrolo-pyrrole polymer semiconductors with branched alkyl side chains. *J. Am. Chem. Soc.* **2011**, *133* (38), 15073–15084.
- (50) Zhang, F.; Wang, S.; Zhu, H.; Liu, X.; Liu, H.; Li, X.; Xiao, Y.; Zakeeruddin, S. M.; Grätzel, M. Impact of Peripheral Groups on Phenothiazine-Based Hole-Transporting Materials for Perovskite Solar Cells. *ACS Energy Letters* **2018**, *3* (5), 1145–1152.
- (51) Zhang, F.; Wang, Z.; Zhu, H.; Pellet, N.; Luo, J.; Yi, C.; Liu, X.; Liu, H.; Wang, S.; Li, X.; et al. Over 20% PCE perovskite solar cells with superior stability achieved by novel and low-cost hole-transporting materials. *Nano Energy* **2017**, *41*, 469–475.
- (52) Xue, Q.; Bai, Y.; Liu, M.; Xia, R.; Hu, Z.; Chen, Z.; Jiang, X.; Huang, F.; Yang, S.; Mastuo, Y.; Yip, H.; Cao, Y.; et al. Dual Interfacial Modifications Enable High Performance Semitransparent Perovskite Solar Cells with Large Open Circuit Voltage and Fill Factor. *Adv. Energy Mater.* **2017**, *7*, 1602333.
- (53) Sun, C.; Wu, Z.; Yip, H.-L.; Zhang, H.; Jiang, X.-F.; Xue, Q.; Hu, Z.; Hu, Z.; Shen, Y.; Wang, M.; et al. Amino-Functionalized Conjugated Polymer as an Efficient Electron Transport Layer for High-Performance Planar-Heterojunction Perovskite Solar Cells. *Adv. Energy Mater.* **2016**, *6* (5), 1501534.

## □ Recommended by ACS

### Approaching the Fill Factor Limit in Dopant-Free Hole Transporting Layer-Based All-Inorganic Perovskite Solar Cells

Kanghui Zheng, Ziyi Ge, et al.

MARCH 10, 2023

ACS APPLIED MATERIALS & INTERFACES

READ ↗

### First-Principles Study of Group VA Monolayer Passivators for Perovskite Solar Cells

Oscar J. Allen, Yun Wang, et al.

MARCH 14, 2023

ACS APPLIED NANO MATERIALS

READ ↗

### Self-Assembled Molecules for Hole-Selective Electrodes in Highly Stable and Efficient Inverted Perovskite Solar Cells with Ultralow Energy Loss

Wenhui Li, Emilio Palomares, et al.

JANUARY 13, 2023

ACS APPLIED ENERGY MATERIALS

READ ↗

### Improving the Thermal Stability of Organic Solar Cells via Crystallinity Control

Qingchun Qi, Long Ye, et al.

DECEMBER 01, 2022

ACS APPLIED ENERGY MATERIALS

READ ↗

Get More Suggestions >